Special Issue

Parker Solar Probe: Ushering a new frontier in space exploration

# Applicability of Taylor's hypothesis during Parker Solar Probe perihelia

Jean C. Perez<sup>1</sup>, Sofiane Bourouaine<sup>1,2</sup>, Christopher H. K. Chen<sup>3</sup>, and Nour E. Raouafi<sup>2</sup>

- Department of Aerospace, Physics and Space Sciences, Florida Institute of Technology, Melbourne, Florida 32901, USA e-mail: jcperez@fit.edu
- <sup>2</sup> Johns Hopkins University Applied Physics Laboratory, Laurel, MD, USA e-mail: sofiane.bourouaine@jhuapl.edu;nour.raouafi@jhuapl.edu
- <sup>3</sup> School of Physics and Astronomy, Queen Mary University of London, London E1 4NS, UK

Received 9 November 2020 / Accepted 24 March 2021

#### **ABSTRACT**

We investigate the validity of Taylor's hypothesis (TH) in the analysis of velocity and magnetic field fluctuations in Alfvénic solar wind streams measured by Parker Solar Probe (PSP) during the first four encounters. The analysis is based on a recent model of the spacetime correlation of magnetohydrodynamic (MHD) turbulence, which has been validated in high-resolution numerical simulations of strong reduced MHD turbulence. We use PSP velocity and magnetic field measurements from 24 h intervals selected from each of the first four encounters. The applicability of TH is investigated by measuring the parameter  $\epsilon = \delta u_0 / \sqrt{2} V_\perp$ , which quantifies the ratio between the typical speed of large-scale fluctuations,  $\delta u_0$ , and the local perpendicular PSP speed in the solar wind frame,  $V_\perp$ . TH is expected to be applicable for  $\epsilon \lesssim 0.5$  when PSP is moving nearly perpendicular to the local magnetic field in the plasma frame, irrespective of the Alfvén Mach number  $M_A = V_{SW}/V_A$ , where  $V_{SW}$  and  $V_A$  are the local solar wind and Alfvén speed, respectively. For the four selected solar wind intervals, we find that between 10 and 60% of the time, the parameter  $\epsilon$  is below 0.2 and the sampling angle (between the spacecraft velocity in the plasma frame and the local magnetic field) is greater than 30°. For angles above 30°, the sampling direction is sufficiently oblique to allow one to reconstruct the reduced energy spectrum  $E(k_\perp)$  of magnetic fluctuations from its measured frequency spectra. The spectral indices determined from power-law fits of the measured frequency spectrum accurately represent the spectral indices associated with the underlying spatial spectrum of turbulent fluctuations in the plasma frame. Aside from a frequency broadening due to large-scale sweeping that requires careful consideration, the spatial spectrum can be recovered to obtain the distribution of fluctuation's energy across scales in the plasma frame.

Key words. solar wind – Sun: heliosphere – turbulence – magnetohydrodynamics (MHD) – plasmas

### 1. Introduction

The analysis of spacecraft signals invariably requires a number of assumptions to properly interpret temporal variations in terms of their corresponding spacetime variations in the plasma frame of reference, defined as the frame where the mean plasma bulk velocity is zero. The most common assumption used in the analysis of turbulent signals far from the Sun is the well-known Taylor's hypothesis (TH) (Taylor 1938), which posits that the temporal variation of spacecraft signals simply arises from the advection of "frozen" structures by the measuring probe. Although TH is almost universally assumed, implicitly or explicitly, in most analyses of solar wind observations (Bruno & Carbone 2013; Chen 2016), its accuracy and applicability to the interpretation of spacecraft observations is still not completely understood (Narita 2017).

The use of TH in solar wind observations is often justified on the simple assumption that the relevant characteristic speeds associated with linear and nonlinear processes in the plasma frame, such as the typical root-mean-squared (rms) speed  $\delta u_0$  at the injection scale and Alfvén speed  $V_A$ , are much smaller that the solar wind speed  $V_{SW}$  (Matthaeus & Goldstein 1982; Perri & Balogh 2010). When  $V_{SW} \gg \delta u_0$ ,  $V_A$ , the plasma dynamics is assumed to be "frozen" in the plasma frame, and therefore

standard correlation and spectral analysis of time signals is directly interpreted as spatial analysis, where the time t can be associated with spatial coordinate  $s = -V_{\rm SW}t$  in the "upstream" direction  $(-V_{\rm SW})$ , which near 1 au is mostly antiradial<sup>1</sup>. This relationship between space and time also implies a relationship between the frequency and wavevector,  $\omega = k \cdot V_{\rm SW}$ , commonly used in the interpretation of frequency spectra of turbulent fluctuations in the solar wind. This frequency-wavevector relation is easily understood because when the magnetic field is approximately time-independent in the plasma frame, spacecraft frequencies  $\omega = k_s V_{\rm SW}$  are mostly due to the Doppler-shift of zero plasma-frame frequencies. Here,  $k_s$  is the "streamwise" component of the wave vector in the plasma frame.

As Parker Solar Probe (PSP) (Fox et al. 2016) reaches closer to the Sun, TH may lead to less accurate or even invalid results (Klein et al. 2014; Bourouaine & Perez 2018), and thus a new methodology is needed to interpret PSP observations beyond TH. The expectation that TH may not be valid for PSP measurements in the near-Sun solar wind has spurred a renewed interest in the fundamentals of the applicability of TH

<sup>&</sup>lt;sup>1</sup> We note that the negative sign comes from the fact that in reality s = Vt, where V is the spacecraft velocity in the plasma frame, which near Earth is  $V = -V_{SW}$ .

to solar wind observations and how the analysis of solar wind signals may differ for PSP measurements (Howes et al. 2014; Klein et al. 2014, 2015; Narita 2017; Bourouaine & Perez 2018, 2019; Huang & Sahraoui 2019; Chhiber et al. 2019; Perez & Bourouaine 2020). A few of these works, which are based on specific assumptions that apply to Alfvénic turbulence, have suggested that under certain conditions, TH may still hold even when  $V_{\rm SW} \sim V_{\rm A}$  (Klein et al. 2014; Bourouaine & Perez 2019).

Bourouaine & Perez (2019, hereafter BP19), propose a new methodology to interpret turbulent signals beyond TH based on a recent model of the spacetime correlation of magnetohydrodynamic (MHD) turbulence, which was validated for strong MHD turbulence in high-resolution numerical simulations of reduced MHD (RMHD) turbulence (Perez & Bourouaine 2020). This new methodology, which assumes that the turbulence is Alfvénic and highly anisotropic  $(k_{\parallel}/k_{\perp} \ll 1 \text{ where } k_{\parallel} \text{ and } k_{\perp}$ are the parallel and perpendicular components of the wavevector with respect to the magnetic field), depends on a single dimensionless parameter  $\epsilon = \delta u_0 / \sqrt{2} V_{\perp}$ , where  $\delta u_0$  is the rms value of the outer-scale fluid velocity (above the onset of the inertial range) and  $V_{\perp}$  is the field-perpendicular velocity of the spacecraft in the plasma frame. TH is recovered in this model in the limit when  $\epsilon \to 0$ , independent of the Alfvén Mach number  $M_A = V_{SW}/V_A$ . Bourouaine & Perez (2020) successfully applied this methodology to *Helios* observations near 0.6 au and found that spectral power laws can be reliably measured as long as  $\epsilon$ remains below 0.5. It is still unknown whether or not this relationship is applicable to PSP observations near perihelia, which motivates the present work.

In this work, we investigate the validity of TH in the first close encounters of PSP in the framework of the BP19 methodology and evaluate the validity (and accuracy) of the TH hypothesis by empirically estimating the dimensionless parameter  $\epsilon$  for selected intervals during the first four encounters. This paper is organized as follows. In Sect. 2 we briefly summarize the BP19 model for the analysis of turbulent signals without assuming TH and discuss how it differs from recently related works. In Sect. 3 we describe the PSP data and methodology for the analysis of power spectral density of magnetic fluctuations in the context of the BP19 model. In Sect. 4 we present the results of our analysis and in Sect. 5 we conclude.

## 2. Analysis of turbulent measurements beyond TH

For noncompressible and transverse Alfvén-like velocity  $\delta v$  and magnetic field  $\delta B$  fluctuations, Kraichnan's idealized sweeping model of hydrodynamics (Kraichnan 1965; Wilczek & Narita 2012) was extended to strong MHD turbulence (Bourouaine & Perez 2019; Perez & Bourouaine 2020) to model the spacetime correlation function of Elsasser fields,  $z^{\pm} \equiv \delta v \pm \delta B/\sqrt{4\pi\rho}$ , where  $\rho$  is the plasma mass density. In this model, the spacetime correlation function is predominantly the result of the sweeping of small-scale fluctuations by large-scale ones, a hypothesis that was thoroughly validated against numerical simulations of RMHD turbulence (Perez & Bourouaine 2020). One key feature of this model is that fluctuating fields are split into outer-scale and small-scale fluctuations, that is, it is assumed that

$$\mathbf{v} = \mathbf{v}' + \delta \mathbf{v}, \quad \mathbf{B} = \mathbf{B}' + \delta \mathbf{B},$$
 (1)

where primed variables, such as v' and B', are considered to be random variables describing eddies in the energy containing

range (or outer scale) with known probability distribution functions, and  $\delta v$ ,  $\delta B$  represent fluctuations at smaller scales. The role of the outer-scale velocity is to produce random advection (sweeping) of small-scale structures, while the role of the outerscale magnetic field is to randomly modify the background to provide a "local magnetic field" along which small-scale fluctuations propagate, which defines the field-parallel direction. An important question that one may ask is how far below the inertial range is Kraichnan's sweeping hypothesis valid. Due to the phenomenological nature of sweeping models, both for HD and MHD, a quantitative answer is not possible. However, numerical simulations have validated the sweeping effect in HD (He & Zhang 2006; Verma et al. 2020) as well as in MHD (Perez & Bourouaine 2020). In the latter case, the sweeping effect is observed to be present at scales that are approximately below one quarter of the outer scale, defined at the onset of the inertial range. Lastly, it is worth mentioning that spacetime correlations and the turbulence decorrelation time have been investigated in the context of the MHD turbulence by a number of authors (Zhou 2010; Matthaeus et al. 2010, 2016; Servidio et al. 2011; Narita et al. 2013; Weygand et al. 2013; Narita 2017) and recently in the framework of weak MHD turbulence (Perez et al. 2020). The main difference that the model of the spacetime correlation in the works of Bourouaine & Perez (2019) and Perez & Bourouaine (2020) have compared with previous works is that the sweeping effect is purely hydrodynamic.

The relation between the spacecraft frequency spectrum,  $P_{\rm sc}^{\pm}(\omega)$ , and the three-dimensional power spectrum,  $P^{\pm}(k_{\perp},k_{\parallel})$ , in the plasma frame that follows from this "sweeping" model has the form

$$P_{\rm sc}^{\pm}(\omega) = \int \frac{P^{\pm}(\mathbf{k}_{\perp}, k_{\parallel})}{\epsilon k_{\perp} V} g\left(\frac{\omega + \mathbf{k}_{\perp} \cdot \mathbf{V}_{\perp} + k_{\parallel} V_{\parallel}}{\epsilon k_{\perp} V}\right) d^{2}k_{\perp} dk_{\parallel}, \qquad (2)$$

where  $\epsilon \equiv \delta u_0/\sqrt{2}V$ ,  $\delta u_0$  is the rms value of the velocity (v') of the energy-containing eddies, and g(x) is the probability density distribution of velocities in the energy-containing range along a given direction  $\hat{n}$ , where  $x \equiv \sqrt{2}v_n'/\delta u_0$  denotes the velocity component  $(v_n')$  normalized to its rms value  $\delta u_0/\sqrt{2}$ . For the solar wind, it is typically found that g(x) is very close to Gaussian (Bruno & Carbone 2013). The dimensionless quantity  $\epsilon$  provides a convenient parameter to assess the validity of the TH hypothesis, which corresponds to the limit  $\epsilon \to 0$ 

$$\lim_{\epsilon \to 0} \frac{1}{\epsilon k_{\perp} V} g\left(\frac{\omega + \mathbf{k}_{\perp} \cdot \mathbf{V}_{\perp} + k_{\parallel} V_{\parallel}}{\epsilon k_{\perp} V}\right) = \delta(\omega + \mathbf{k}_{\perp} \cdot \mathbf{V}_{\perp} + k_{\parallel} V_{\parallel}). \quad (3)$$

It is important to note that the validity of Eq. (3) does not require  $M_A \gg 1$ , as long as the turbulence is strongly anisotropic. Remarkably, the transformation kernel in Eq. (2) is found to be the same for both Elsasser fields  $z^{\pm}$ , independent of crosshelicity. Fundamentally, the reason that this transformation is the same for both Elsasser fields is because it is determined entirely by sweeping from the same velocity field, v', of the energy-containing scales. Therefore, hereafter we omit the labels " $\pm$ " as the following analysis is the same for both Elsasser fields  $z^{\pm}$ .

This relation can be reduced to a simpler expression connecting spacecraft frequencies to the field-perpendicular wavevector  $k_{\perp}$  by making the following assumptions: (1) the three-dimensional power spectrum  $P = P(k_{\perp}, k_{\parallel})$  is nearly isotropic in the field perpendicular plane, that is, it does not depend on the orientation of  $k_{\perp}$ ; (2) the spectrum  $P(k_{\perp}, k_{\parallel})$  is strongly anisotropic with respect to the magnetic field direction, that is to say it is nearly zero unless  $k_{\parallel} \ll k_{\perp}$ ; and (3) the spacecraft

Table 1. Selected 24 h intervals used in our analysis, one from each of the first four encounters E1 to E4.

Encounter	Interval	r (au)	Plasma instrument	
E1	2018-11-05 15:30 to 2018-11-06 15:30	0.166	SPC	
E2	2019-04-04 16:00 to 2019-04-05 16:00	0.166	SPC	
E3	2019-08-29 12:00 to 2019-08-30 12:00	0.191	SPC	
E4	2020-01-28 14:30 to 2020-01-29 14:30	0.131	SPAN-ion	

**Notes.** We note that *r* represents the average heliocentric distance for each interval. The last column indicates the primary instrument used in the analysis of plasma moments. With the exception of E3, all intervals were selected to be near PSP perihelia.

velocity in the plasma frame V is "sufficiently oblique", in other words it satisfies  $V_{\perp}/V_{\parallel} \gg k_{\parallel}/k_{\perp}$ . The first two assumptions are based on theoretical predictions from a number of phenomenological models of MHD turbulence (Goldreich & Sridhar 1995; Boldyrev 2005, 2006; Chandran 2008; Perez & Boldyrev 2009), which have been verified in high-resolution numerical simulations (Müller & Grappin 2005; Mason et al. 2006; Perez et al. 2012), and they are expected to be present in solar wind observations (Bieber et al. 1996; Saur & Bieber 1999; Horbury et al. 2008; Wicks et al. 2010; Chen et al. 2011, 2012). The third assumption simply requires that the sampling angle  $\theta_{VB}$ , defined as the angle between the spacecraft velocity in the plasma frame and the magnetic field ( $\tan \theta_{\rm VB} \equiv V_{\perp}/V_{\parallel}$ ), be much larger than a critical angle  $\theta_c$  determined by the anisotropy  $\tan \theta_c \sim k_{\parallel}/k_{\perp}$ , which is expected to be small for strongly anisotropic turbulence. However, because PSP observations are single-point measurements, an empirical determination of this critical angle is not straightforward. For simplicity, we provide an empirical estimate of this critical angle by assuming the turbulence is critically balanced (Goldreich & Sridhar 1995), that is, the Alfvén propagation time is of the same order as the nonlinear energy-cascade time at each scale  $l \sim 1/k_{\perp}$  in the inertial range,  $k_{\parallel}V_{\rm A} \sim k_{\perp}\delta v_l$ , when the turbulence cascade is strong. In this critically-balanced state, the energy predominantly cascades to small perpendicular scales, resulting in a scale-dependent anisotropy in which  $k_\parallel/k_\perp$ becomes smaller at smaller scales. We thus estimated  $k_{\parallel}/k_{\perp} \sim$  $\delta u_0/V_A \equiv \tan \theta_c$  using  $\delta u_0$  at the outer scale, which provides an overestimate of the critical angle. Under these three assumptions, the relation between the frequency power spectrum as measured by the spacecraft and the reduced field-perpendicular spectrum  $E(k_{\perp}) = \int_{-\infty}^{\infty} 2\pi k_{\perp} P(k_{\perp}, k_{\parallel}) dk_{\parallel}$  is (Bourouaine & Perez 2019)

$$P_{\rm sc}(\omega) = \int_0^\infty E(k_\perp) \frac{\bar{g}_{\epsilon} (\omega/k_\perp V_\perp)}{k_\perp V_\perp} dk_\perp, \tag{4}$$

where

$$\bar{g}_{\epsilon}(x) = \frac{2}{\pi} \int_{0}^{\pi} \frac{1}{\epsilon} g\left(\frac{x + \cos\phi}{\epsilon}\right) d\phi \tag{5}$$

results from the integration over the angle  $\phi$  in the scalar product  $k_{\perp} \cdot V_{\perp} = k_{\perp} V_{\perp} \cos \phi$ . We note that because we are neglecting the parallel spacecraft velocity,  $V_{\parallel}$ , we use  $V_{\perp}$  to define  $\epsilon = \delta u_0 / \sqrt{2} V_{\perp}$  instead of the spacecraft speed V. For a power-law spectrum  $E(k_{\perp}) = C k_{\perp}^{-\alpha}$ , using the change of variables  $x = \omega / k_{\perp} V_{\perp}$ , Eq. (4) becomes

$$P_{\rm sc}(\omega) = \frac{\Lambda_{\alpha,\epsilon}}{V_{\perp}} E\left(\omega/V_{\perp}\right),\tag{6}$$

where

$$\Lambda_{\alpha,\epsilon} \equiv \int_0^\infty f_{\alpha,\epsilon}(x) dx, \qquad f_{\alpha,\epsilon}(x) \equiv x^{\alpha-1} \bar{g}_{\epsilon}(x). \tag{7}$$

Equation (6) shows that the frequency power spectrum exhibits the same power law of the underlying spatial energy spectrum  $E(k_{\perp})$ , even when TH does not hold. Although a similar result was also found by Wilczek & Narita (2012) and Narita (2017), an important difference with BP19 is that the broadening parameter  $\epsilon$  is controlled by pure HD sweeping and therefore the scaling factor  $\Lambda_{\alpha,\epsilon}$  is the same for both  $z^+$  and  $z^-$ . It is worth mentioning that although the model was derived for Elsasser fluctuations, it can be extended to velocity and magnetic field fluctuations.

The scaling factor  $\Lambda_{\alpha,\epsilon}$  can be calculated once empirical values of  $\alpha$  and  $\epsilon$  are determined. Therefore, the analysis of turbulent power laws from spacecraft measurements in this framework requires the accurate estimation of  $\alpha$ ,  $\delta u_0$ , and  $V_{\perp}$ . Bourouaine & Perez (2020) applied this methodology to a three-day interval at 0.6 au from Helios measurements, and they found that for the observed values of  $\epsilon \lesssim 0.1$ , the empirical value for  $\Lambda_{\alpha,\epsilon}$ remained close enough to the value expected when TH is valid, approximately  $\Lambda_{TH} \simeq 0.7628$  for  $\alpha = 3/2$  and  $\Lambda_{TH} \simeq 0.7132$  for  $\alpha = 5/3$ . In this case, TH can still be applied to reconstruct the reduced perpendicular energy spectrum, as long as the sampling angle  $(\theta_{VB})$  is much greater than 20°. If the spacecraft velocity is below this critical angle, which defines the acceptable "obliqueness" of the spacecraft, a different analysis that involves the field-parallel components of the wavevector and the spacecraft velocity is required.

# 3. Data description and methodology

We used PSP velocity and magnetic field measurements from a set of 24 h intervals, shown in Table 1, during the first four close encounters covering heliocentric distances between 0.13 au to 0.19 au to test the validity of TH near PSP perihelia. Proton number density and velocity were obtained from the moments of the velocity distribution functions measured by the Solar Probe Cup (SPC) and the SPAN-ion on board the SWEAP instrument suite (Kasper et al. 2016). The choice between SPC and SPAN-ion signals was made based on which instrument has the best field-of-view (FOV) for each interval we analyzed (see Table 1), while for those cases where it is not clear which instrument provides a better estimate of the moments, our analysis was performed with both signals to determine the sensitivity of our analysis to discrepancies between SPC and SPAN measurements. Magnetic field measurements were obtained from the fluxgate magnetometer (MAG) on board the FIELDS instrument suite (Bale et al. 2016). Velocity and magnetic field measurements, which were sampled with an average resolution of 0.874 s and 0.22 s, respectively, were resampled on the same temporal grid by averaging over a 1 s window. Figure 1 shows time signals of proton number density, radial and tangential velocity from SPC and SPAN-ion measurements, and magnetic field

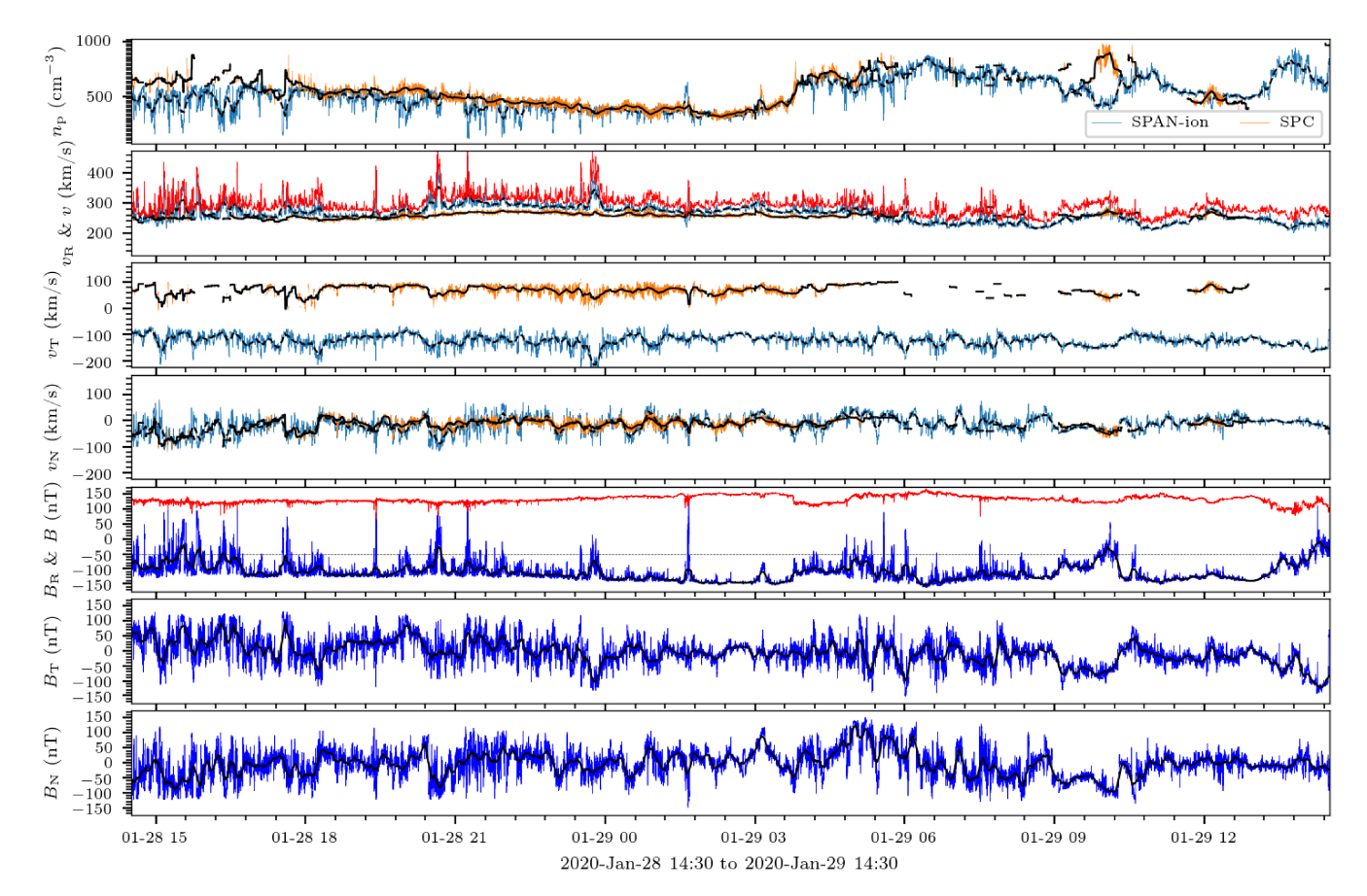


**Fig. 1.** 24 h PSP interval between 2020 Jan 28 at 14:30 and 2020 Jan 29 at 14:30. *Top panel*: proton number density as measured by both SPC and SPAN-ion. *Second to fourth panels*: (*from top to bottom*) bulk plasma velocity in the radial (R), tangential (T), and normal (N) directions, respectively. *Three bottom panels*: R, T, and N components of the magnetic field. The red line in the *second and fifth panels* represents the solar wind speed and the magnitude of the magnetic field, respectively. During encounter E4, due to the high PSP's high speed at perihelion, a larger fraction of solar wind particles fall under SPAN-ion's than on SPC's field-of-view (FOV).

measurements during a day-long interval a few days before the fourth perihelion.

The velocity and magnetic fields in the energy-containing range were obtained by performing the following moving averages over a time window T at each time t

$$\mathbf{v}'(t) = \frac{1}{T} \int_{t-T/2}^{t+T/2} \mathbf{v}(t') dt', \text{ and } \mathbf{B}'(t) = \frac{1}{T} \int_{t-T/2}^{t+T/2} \mathbf{B}(t') dt',$$
 (8)

where T was chosen to correspond to the turbulence outer scale, which we define as the inverse of the spectral break frequency that separates the  $f^{-1}$  range from the inertial range. In other words, we considered  $T=1/f_b$  where  $f_b$  is the frequency at the onset of the inertial range. In the present analysis, we use T=8 min, consistent with spectral break frequency estimates  $f_b \approx 2 \times 10^{-3}$  Hz from the first two encounters (Chen et al. 2020; Parashar et al. 2020). Similar values for the spectral break frequency were also found by Bourouaine et al. (2020) when the power spectra were calculated within and outside the so-called SwitchBacks (SBs) (Bale et al. 2019; Kasper et al. 2019), although larger values of  $f_b \approx 2 \times 10^{-2}$  have been reported outside SB regions (Dudok de Wit et al. 2020). The moving averages defined in Eq. (8), which act as a low-pass filter that removes fluctuations below the timescale T, lead to smoother random time signals plotted as black lines in Fig. 1, representing the large-scale component of the corresponding quantities in the interval E4 described in Table 1. In the figure, dash lines

correspond to SPAN-ion measurements and solid lines correspond to SPC.

Once the time signals for the outer scale velocity fluctuations were obtained, their mean and rms values

$$V_{SW} = \langle v' \rangle, \qquad \delta u_0^2 = \langle |v'|^2 \rangle - |V_{SW}|^2,$$
 (9)

were calculated, respectively. Here  $\langle \cdots \rangle$  represents a suitable ensemble averaging procedure, which in practice is replaced by a temporal average under the assumption of ergodicity. The rms velocity  $\delta u_0$  represents the root-mean-squared value of the bulk velocity associated with fluctuations that are larger than T=8 min, which can also be obtained from the total fluctuation energy between f=0 to  $f=f_{\rm b}$ , as calculated by Bourouaine & Perez (2020). Lastly, we determined the spacecraft velocity in the plasma frame V and its angle with respect to the local magnetic field  $\theta_{\rm VB}$ 

$$V = V_{\rm sc} - V_{\rm SW}$$
 and  $\theta_{\rm VB}(t) = \arccos\left(\hat{\boldsymbol{V}} \cdot \hat{\boldsymbol{B}}'(t)\right)$ , (10)

where  $\hat{V}$  and  $\hat{B}'$  represent unit vectors in the direction of V and B', respectively. We note that because the local magnetic field B'(t) is fluctuating, one obtains a distribution of angles corresponding to turbulent "realizations" at each time t.

Equation (6) allows one to reconstruct the reduced energy spectrum  $E(k_{\perp})$  from the spacecraft frequency spectrum  $P_{\rm sc}(\omega)$  as long as one considers measurements where the sampling angle

**Table 2.** Relevant empirical parameters for the four 24 h intervals in Table 1 used in our analysis.

Encounter	$V  (\mathrm{km}  \mathrm{s}^{-1})$	$\delta u_0  (\mathrm{km}  \mathrm{s}^{-1})$	$V_{\rm A}~({\rm km~s^{-1}})$	$M_{\mathrm{A}}$	$\theta_{ m c}$	χ <sub>c</sub> (%)	$\chi_{30}(\%)$	$\epsilon_{ m c}$	$\epsilon_{30}$
E1	315	40	82	3.8	23°	56	43	0.24	0.19
E2	400	37	182	2.2	12°	63	10	0.34	0.14
E3	490	49	157	3.1	$17^{\circ}$	52	18	0.25	0.15
E4	300	38	114	2.6	$22^{\circ}$	92	57	0.19	0.14

**Notes.** We note that V is the average spacecraft speed in the solar wind frame,  $\delta u_0$  is the rms value of velocity at the large-scale (T = 8 min),  $\theta_c$  is the critical angle above which the spacecraft can be considered nearly perpendicular to the local field,  $\chi_c$  is the fraction of the interval in which the sampling angle is above the critical angle  $\theta_c$ , and  $\chi_{30}$  is the fraction of the interval in which the sampling angle is above 30°.

is much larger than the critical angle  $\tan\theta_{\rm c} \approx \delta u_0/V_{\rm A}$ . Because  $V_{\perp}$ , and therefore  $\epsilon$ , depends on the sampling angle  $\theta_{\rm VB}$ , we classify measurements at each time t into ten-degree angular bins  $\Delta\theta=10^{\circ}$  centered around  $\theta_i=10^{\circ}-90^{\circ}$  in increments of  $10^{\circ}$ .

The temporal autocovariance of magnetic field signals<sup>2</sup>  $b(t) \equiv B(t)/\sqrt{4\pi\rho}$  was calculated for each sampling angle range using conditioned correlation functions (Bourouaine & Perez 2020; Bourouaine et al. 2020)

$$C(\tau, \theta_{\rm VB}) = \langle \boldsymbol{b}(t) \cdot \boldsymbol{b}(t+\tau) \rangle_{\theta_{\rm VB}}, \qquad (11)$$

where the ensemble average was calculated by averaging over those times t for which the angle  $\theta_{VB}$  fell within each of the angle bins defined above. From there, a frequency spectrum was obtained for each angle

$$P_{\rm sc}(\omega, \theta_{\rm VB}) = \frac{1}{2\pi} \int_{-\infty}^{\infty} C(\tau, \theta_{\rm VB}) e^{i\omega\tau} d\tau. \tag{12}$$

If the assumption of anisotropy and oblique sampling direction are satisfied, all  $P_{\rm sc}(\omega,\theta_{\rm VB})$  spectra should result in the same spatial spectrum  $E(k_\perp)$  independent of the sampling angle (Bourouaine & Perez 2020). It then follows from Eq. (6) that

$$E(\omega/\lambda V_{\perp}) = \lambda V_{\perp} P_{\rm sc}(\omega), \tag{13}$$

where  $\lambda \equiv \Lambda^{1/(\alpha-1)}$ . This last expression shows that the spatial power spectrum can be reconstructed from the frequency power spectrum by using the rescalings  $k_{\perp} = \omega/\lambda V_{\perp}$  and  $E = \lambda V_{\perp} P_{\rm sc}$ . It is worth noting that although the expression  $k_{\perp} = \omega/\lambda V_{\perp}$  provides a connection between the frequency and wavenumber, it should not be interpreted in the same way as when the standard TH applies. When TH is not valid, the fluctuation energy within a narrow frequency range around each spacecraft frequency  $\omega$  cannot be associated with a narrow range of wavevectors around a single wavevector in the plasma frame. In the present case, the transformations  $k_{\perp} = \omega/\lambda V_{\perp}$  and  $E = \lambda V_{\perp} P_{\rm sc}$  simply provide a way to reconstruct the spatial power spectrum in terms of  $k_{\perp}$  from the measured  $P_{\rm sc}(\omega)$  at each angle  $\theta_{\rm VB}$ .

## 4. Results

### 4.1. Empirical evaluation of $\epsilon$ in the first four encounters

Table 2 shows the most relevant parameters, within the methodology described in the previous section, obtained empirically for all intervals considered in this work. For encounters E1 to E3, plasma measurements from the SPC instrument were used

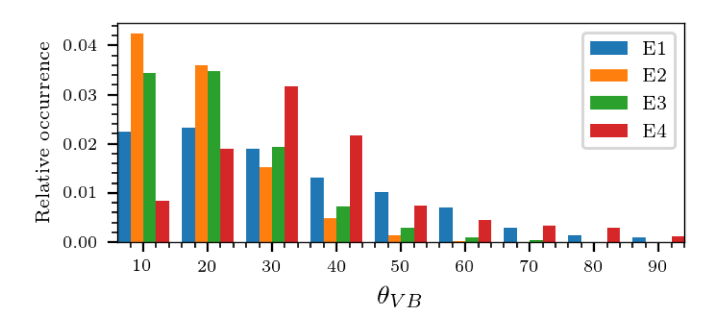


Fig. 2. Normalized histograms showing the distribution of the sampling angle  $\theta_{VB}$  defined in Eq. (10) for selected 24 h intervals, one for each encounter from E1 to E4. The histograms indicate that for the selected intervals, small sampling angles have the highest occurrence, indicating that the spacecraft is often traveling nearly parallel to the local magnetic field. However, sampling angles above the critical angles shown in Table 1 occur more than 50% of the time.

in the analysis, while plasma measurements from the SPAN-ion instrument were used in the analysis of encounter E4.

The average spacecraft speed measured in the plasma frame ranges from 300 to nearly 500 km s<sup>-1</sup>, so that the interval selection covers both slow and fast solar wind streams. The rms of the velocity at the outer scale ranges from 40 to 52 km s<sup>-1</sup>, and it is much smaller than the spacecraft motion. The average Alfvén Mach number  $M_A$  is found between two and four, which means that under the usual assumptions, TH would be marginally applied at best, given that  $M_A$  is not much larger than one. However, because our analysis is based on the assumptions in the BP19 methodology, we do not require this as a condition. One condition that the BP19 methodology does require is that one can only consider intervals for which the sampling angle is greater that the critical angle  $\tan \theta_c \sim \delta u_0/V_A$  (assuming the turbulence is critically balanced), which we empirically find in the range from  $10^{\circ}$  to  $20^{\circ}$  for the four intervals we consider.

Figure 2 shows the distribution of sampling angles  $\theta_{VB}$  resulting from our analysis of all four intervals. It is observed that for a substantial portion of the signal, the sampling direction is between  $10^{\circ}$  and  $20^{\circ}$ , indicating that PSP is very often flying nearly parallel to the local magnetic field. For these small angles, the methodology described above does not apply and it requires further investigation.

In order to quantify how often the spacecraft is sampling at a given angle, we define  $\chi(\theta)$  as the fraction of the time in which the sampling angle is above a certain value  $\theta$ 

$$\chi(\theta) \equiv \frac{\text{Number of samples where } \theta_{\text{VB}} \ge \theta}{N_{\text{total}}},$$
(14)

where  $N_{\text{tot}}$  is the total number of samples. By a sample (or count), we mean an individual PSP measurement out of the

 $<sup>^2</sup>$  We converted magnetic field signals to fluctuating Alfvén velocity using the local average plasma density.

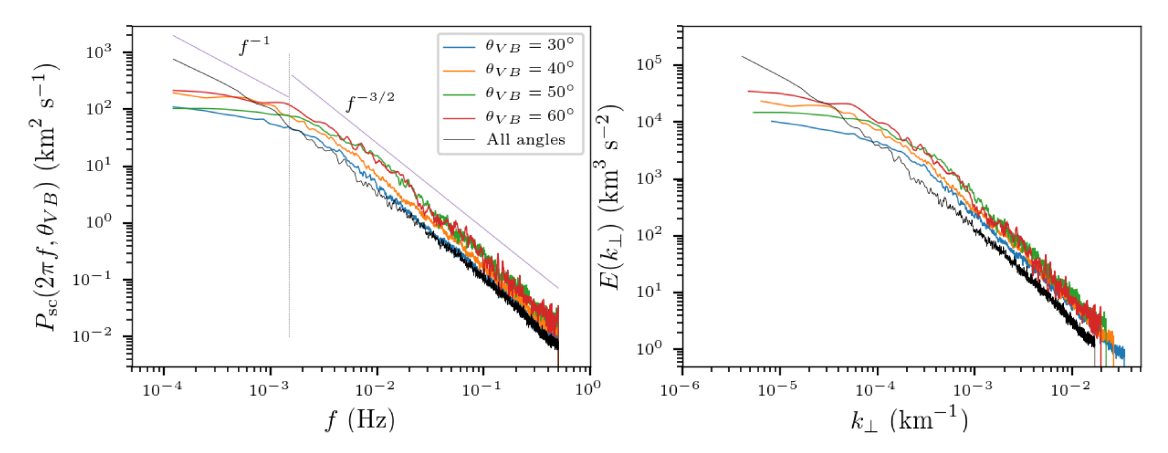


Fig. 3. Left: frequency spectrum of magnetic fluctuations  $P_{\rm sc}(\omega, \theta_{\rm VB})$  for angles  $\theta_{\rm VB} = 30^\circ$ ,  $40^\circ$ ,  $50^\circ$ , and  $60^\circ$  corresponding to interval E4, as well as the full spectrum irrespective of the angle. The spectral break between the 1/f and  $f^{-3/2}$  ranges for the unconditioned spectrum (black line) is found approximately (by inspection) at  $f_b \approx 2 \times 10^{-3}$  Hz, indicated by the vertical dotted line. Right: spatial energy spectrum of magnetic fluctuations  $E(k_\perp)$  reconstructed from the frequency spectra  $P_{\rm sc}(\omega, \theta_{\rm VB})$  for each sampling angle as well as by using the standard TH (black line).

86 400 records available in any 24 h interval at 1 s resolution. Table 2 shows that the fraction of samples above the critical angle,  $\chi_c$ , comprise roughly 50–90% of the total count, allowing for at least one half of each interval for statistical analysis. However, we restricted the analysis to angles at or above 30°, for which the fractions  $\chi_{30}$ , shown in Table 2, are much lower and particularly worse for encounters E2 and E3. For the empirical values of  $\delta u_0$  and V shown in Table 2, we can determine  $\epsilon$  as a function of the sampling angle  $\theta_{VB}$ 

$$\epsilon = \frac{\delta u_0}{\sqrt{2}V_{\perp}} = \frac{\delta u_0}{\sqrt{2}V\sin\theta_{\rm VB}} \tag{15}$$

and obtain the values of  $\epsilon$  at the critical angle ( $\epsilon_c$ ) and at the smallest angle that we consider in the present analysis ( $\epsilon_{30}$ ). We found that  $\epsilon_c \le 0.35$  and  $\epsilon_{30} \le 0.2$  across all intervals, which is below the acceptable level of 0.5 obtained by Bourouaine & Perez (2020).

## 4.2. Reconstructing field-perpendicular spectrum $E(k_{\perp})$

In the following, we proceed to reconstruct the reduced energy spectrum  $E(k_\perp)$  using data from within each angle bin above  $30^\circ$  and for which we find a large statistical sample. For illustration purposes, we concentrate on a 24 h interval just before the fourth perihelion (E4), which was also investigated using standard TH analysis by Chen et al. (2021). Table 3 shows the values of  $\epsilon$ ,  $V_\perp$ , and the number of statistical samples (counts) associated with this interval for each ten-degree angle bin around  $30^\circ$ ,  $40^\circ$ ,  $50^\circ$ , and  $60^\circ$ . In this statistical sample,  $\epsilon \leq 0.2$ , in which case the BP19 methodology in the TH limit ( $\epsilon \to 0$ ) is applicable, that is, combining Eqs. (2) and (3) leads to

$$P_{\rm sc}(\omega) = \int P(\mathbf{k})\delta(\omega + \mathbf{k} \cdot \mathbf{V})d^3k. \tag{16}$$

The most common form of TH follows from this expression by performing the integral in a Cartesian coordinate system with one axis along the streamwise direction so that

$$P_{\rm sc}(\omega) = \frac{1}{V} \int_{-\infty}^{\infty} E_{1D}(k_{\rm s}) \delta(k_{\rm s} + \omega/V) dk_{\rm s} = \frac{1}{V} E_{1D}(\omega/V). \tag{17}$$

Here  $E_{1D}(k_s)$  is the one-dimensional energy spectrum with respect to the streamwise (sampling) direction. This expression

**Table 3.** Relevant parameters for each angle bin considered in our analysis with a sufficiently large number of samples.

$\theta_{\rm VB}$ (degrees)	$\epsilon$	$V_{\perp}  (\mathrm{km}  \mathrm{s}^{-1})$	Counts	$\Lambda_{lpha,\epsilon}$
30	0.20	198	14 305	0.7667
40	0.15	254	6690	0.7649
50	0.13	303	5548	0.7644
60	0.11	342	3630	0.7639

**Notes.** The parameter  $\epsilon$  remains below 0.15, which allows for the application of the TH in the framework of BP19. For reference, at 1 s resolution, the total number of counts in any given 24 h interval is 86 400 samples. It is also important to note that values for  $\Lambda_{\alpha,\epsilon}$  were calculated for  $\alpha = 3/2$  and using Eq. (18)  $\Lambda_{\rm TH} \simeq 0.7628$ .

resembles Eq. (6) with  $\Lambda_{\alpha,\epsilon} = 1$  and leads to the familiar  $\omega = -k_s V$  expression to relate spacecraft frequencies with streamwise wavenumber  $k_s$ .

However, because we are interested in reconstructing the angle-integrated field-perpendicular spectrum  $E(k_{\perp})$ , Eq. (16) must be integrated in cylindrical coordinates. Using the change of variables  $x = \omega/k_{\perp}V_{\perp}$ , we obtained<sup>3</sup>

$$P_{\rm sc}(\omega) = \frac{\Lambda_{\rm TH}}{V_{\perp}} E(\omega/V_{\perp}),\tag{18}$$

where

$$\Lambda_{\text{TH}} = \frac{2}{\pi} \int_0^1 f_{\alpha,\text{TH}}(x) dx, \quad f_{\alpha,\text{TH}}(x) = \frac{2}{\pi} \int_0^1 \frac{x^{\alpha - 1}}{\sqrt{1 - x^2}}.$$
 (19)

Again, Eq. (18) also resembles Eq. (6) with  $\Lambda_{\alpha,\epsilon}$  replaced by  $\Lambda_{\rm TH}$ . In fact, it can be shown that  $\Lambda_{\rm TH} = \lim_{\epsilon \to 0} \Lambda_{\alpha,\epsilon}$ , which is consistent with the BP19 model in the limit when  $\epsilon \to 0$ . The scaling factor  $\Lambda_{\rm TH}$  is due to the integration with respect to the angle  $\phi$  in the dot product  $k_{\perp} \cdot V = k_{\perp} V_{\perp} \cos \phi$  (Bourouaine et al. 2012; Bourouaine & Chandran 2013; Martinović et al. 2019).

Using Eqs. (11) and (12) within each statistical sample described in Table 3,  $P_{\rm sc}(\omega, \theta_{VB})$  was calculated for magnetic field measurements  $\boldsymbol{b}(t)$  according to Eq. (12). The left panel of Fig. 3 shows frequency spectra  $P_{\rm sc}(\omega, \theta_{VB})$  for the interval

<sup>&</sup>lt;sup>3</sup> Here it has been further assumed that  $|k_{\parallel}V_{\parallel}| \ll |\mathbf{k}_{\perp} \cdot \mathbf{V}_{\perp}|$ .

in encounter E4 for angles 30°, 40°, 50°, and 60°, as well as the full spectrum without imposing conditions on the angle (all angles). We note that the spectral break frequency  $f_b$  for the unconditioned spectrum (black line) is found (by inspection) approximately at  $2\times 10^{-3}$  Hz, which is consistent with our assumption that the outer scale corresponds to T=8 min. All five frequency spectra are consistent with a spectral index  $\alpha=3/2$  in agreement with a separate analysis of this interval Chen et al. (2021). The right panel shows the reduced energy spectrum  $E(k_\perp)$  reconstructed using Eq. (13) with  $\lambda=\Lambda_{\rm TH}^{1/(\alpha-1)}=\Lambda_{\rm TH}^2\simeq 0.58$ . The scaling factor  $\Lambda_{\alpha,\epsilon}$  calculated for the empirical values of  $\epsilon$  in each interval are found to differ from  $\Lambda_{\rm TH}$  by less than 1%, as shown in Table 3. The right panel of Fig. 3 shows the spatial spectrum  $E(k_\perp)$ , reconstructed from the frequency spectra  $P_{\rm sc}(\omega,\theta_{\rm VB})$  for each sampling angle, as well as the one obtained using the standard TH (black line).

It is important to emphasize that Eq. (13), which follows from Eq. (6), holds only when the power law  $E(k_{\perp})$  extends from  $k_{\perp} = 0$  to  $\infty$ . In solar wind observations, power-law behavior extends over a finite range from  $k_{\min}$  to  $k_{\max}$ , and therefore the integration in Eq. (7) must be performed over the interval  $[x_{\min}, x_{\max}]$ , where  $x_{\min} = \omega/k_{\max}V_{\perp}$  and  $x_{\max} = \omega/k_{\min}V_{\perp}$ . In this case, the parameter  $\Lambda_{\alpha,\epsilon}$  becomes a function of  $\omega$ , and  $P_{\text{sc}}(\omega)$  no longer exhibits the same power law as  $E(k_{\perp})$ . However, because  $f_{\alpha,\epsilon}$  is usually a localized function, it is possible to define an interval  $[x_0, x_1]$ , such that

$$\int_{x_0}^{x_1} f_{\alpha,\epsilon}(x) dx \approx \int_0^\infty f_{\alpha,\epsilon}(x) dx = \Lambda_{\alpha,\epsilon},$$
(20)

in which case Eq. (13) remains approximately valid for frequencies in the range

$$x_1 k_{\min} V_{\perp} \le \omega \le x_0 k_{\max} V_{\perp}. \tag{21}$$

Equation (21) also reveals that the fluctuation energy measured in a narrow frequency bin  $\delta\omega$  around  $\omega$  arises from a broad range of wavenumbers inside the range  $[k_{\min}, k_{\max}]$ , rather than a narrow wavenumber bin  $\delta k$  around a streamwise wavenumber  $k_{\rm s} = \omega/V_{\perp}$ , even in the TH limit when  $\Lambda_{\alpha,\epsilon} \approx \Lambda_{\rm TH}$ . For instance, Fig. 4 shows that the function  $f_{\alpha,\epsilon}(x)$ , for values of  $\epsilon$  similar to those obtained empirically and  $\alpha = 3/2$ , becomes negligibly small above x = 2. It can also be shown that its integral from  $x_0 = 0.25$  to  $x_1 = 1.25$  captures more than 90% of  $\Lambda_{TH}$  for any value of  $\epsilon \leq 0.2$ . In all cases, the largest contribution to the fluctuation energy at a given frequency comes from  $x \approx 1$ , while the overall width of the function  $f_{\alpha,\epsilon}(x)$  increases, somewhat asymmetrically, with increasing  $\epsilon$ . The broadening to the left of x = 1, which affects high frequencies, remains largely unchanged with increasing  $\epsilon$  when compared with the TH limit. On the right side of x = 1, which affects low frequencies, the broadening is most significant for  $\epsilon = 0.2$ . When putting everything together, Eq. (18) approximately holds as long as

$$0.25k_{\min}V_{\perp} \le \omega \le 1.25k_{\max}V_{\perp},\tag{22}$$

assuming  $E(k_{\perp})$  exhibits a power law in the  $[k_{\min}, k_{\max}]$  range. A possible consequence of the substantial broadening to the right of x=1 is that it could play a role in spectral breaks at low frequencies. However, because the model of the spacetime correlation holds for fluctuations with lengthscales that are much smaller than the outer scale and highly anisotropic, the validity of the BP19 phenomenology is less justified for frequencies (or wavenumbers) that are too close to the spectral break between

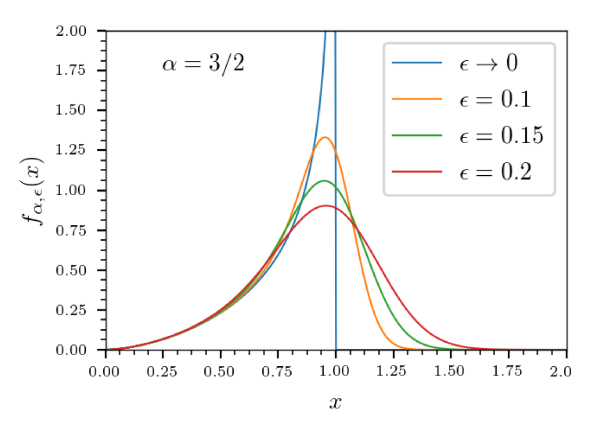


**Fig. 4.** Function  $f_{\alpha,\epsilon}(x)$  for  $\alpha = 3/2$  with  $\epsilon$  values similar to those obtained empirically. It is observed that for  $\epsilon \leq 0.2$  the function peaks around x=1, corresponding to the TH limit, while the broadening around x=1 on the left side of the peak is similar for all  $\epsilon$ . The difference between using the BP19 phenomenology or TH is more pronounced on the right side of the peak, affecting small frequencies.

the 1/f and  $f^{-3/2}$  ranges, where the spectrum is more likely to be isotropic (Wicks et al. 2010, 2011). The validity of the BP19 model for the spacetime correlation has been verified in numerical simulations for inertial-range scales that are approximately below one quarter of the outer scale (or the onset of the inertial range) (Perez & Bourouaine 2020), which is consistent with the lower bound in Eq. (22).

#### 5. Conclusions

In this work, we have presented an analysis of four 24 h intervals during the first four PSP close encounters to investigate the applicability of TH in the framework of a recent methodology (Bourouaine & Perez 2019, 2020). This new methodology is based on a phenomenological "sweeping" model of the spacetime correlation function of MHD turbulence, which was validated against numerical simulations of RMHD turbulence (Perez & Bourouaine 2020). As opposed to previous models of the spacetime correlation (Servidio et al. 2011; Lugones et al. 2016; Narita 2017), the BP19 phenomenology suggests that the temporal decorrelation of small scales is entirely due the random advection by velocity fluctuations in the energy-containing range. The BP19 model is broadly applicable to Alfvénic solar wind streams, such as those recently observed by PSP that are believed to originate from a small equatorial coronal hole measured by PSP (Bale et al. 2019). The validity of TH in this model depends on a single parameter that measures the ratio between the velocity rms of large-scale fluctuations and the spacecraft speed, perpendicular to the local field, with respect to the plasma frame,  $\epsilon = \delta u_0 / V_{\perp} \sqrt{2}$ . The only assumptions in this methodology are that the turbulence is Alfvénic and strong (in the critically balance sense), and that the sampling direction is sufficiently oblique that it can be considered nearly perpendicular to the field. Solar wind observations have been found to be largely consistent with a critically-balanced nonlinear cascade and its associated spectral anisotropy, see for instance (Horbury et al. 2008; Chen et al. 2011; von Papen & Saur 2015). Under these conditions, the TH hypothesis is expected to remain as a good approximation as long as  $\epsilon \leq 0.5$  (Bourouaine & Perez 2020).

In our analysis, we found that for the intervals we considered during the first four perihelia, the parameter  $\epsilon$  remains below 0.2 at sampling angles greater than 30°, which can be considered sufficiently oblique. For these values of  $\epsilon$ , TH is found to hold, irrespective of the value of the Alfvén Mach

number  $M_A$ . Although TH remains approximately valid, in the sense that the frequency spectrum can be interpreted as the one-dimensional spatial energy spectrum with respect to the streamwise direction, the frequency spectrum was used to reconstruct the field-perpendicular energy spectrum  $E(k_\perp)$ , which measures the spectral energy distribution of the turbulence with respect to the angle-integrated wavenumber  $k_\perp$ . When TH is used to recover  $E(k_\perp)$ , a frequency broadening similar to the one obtained in the BP19 phenomenology arises, resulting in an overall decrease in the fluctuation power at each frequency. For the empirical values of  $\epsilon$ , below 0.2, the broadening is very similar whether TH or the BP19 methodology is used.

The methodology we presented to reconstruct the spatial energy spectrum from measurements of the frequency spectrum in the spacecraft frame can be applied to measurements from future perihelia closer to the Sun, where one expects the value of  $\epsilon$  to be larger. This methodology can be summarized in the following straightforward steps:

- 1. The timescale  $T = 1/f_b$  corresponding to the onset of the inertial range of velocity fluctuations is obtained from the spectral break frequency  $f_b$  that separates the  $f^{-1}$  from the inertial range.
- 2. Temporal signals for the outer-scale velocity v' and magnetic field B' are obtained via the moving averages defined in Eqs. (8). Mean and rms values for these signals are obtained, according to Eqs. (9).
- 3. The  $\theta_{VB}(t)$  signal is calculated from Eqs. (10) and used to group PSP measurements into angular bins of  $\Delta\theta = 10^{\circ}$  around angles  $\theta_i = 10^{\circ}, 20^{\circ}, \dots, 90^{\circ}$ . In order to obtain reliable averages, the selected intervals must be long enough to contain a large statistical sample in each angular bin. Figure 2 shows that the number of samples becomes smaller with increasing  $\theta_{VB}$ .
- 4. The value of the  $\epsilon$  parameter as a function of the sampling angle  $\theta_{VB}$  is calculated from Eq. (15)
- 5. Conditioned correlation functions, as defined by Eq. (11), are calculated. Resulting correlations are used to compute the power spectral density (PSD) via the Fourier transform. A reliable estimate of  $C(\tau, \theta_{VB})$  requires a large number of statistical samples at each  $\tau$  and the correlation drops to nearly zero for the largest time lag  $\tau$ .
- 6. The spatial spectrum  $E(k_{\perp})$  is obtained from Eq. (13) for each angle. If the anisotropy assumption is correct and the sampling angle sufficiently oblique, the reconstructed spectrum should be independent of the angle (Bourouaine & Perez 2020), as seen in Fig. 3. The agreement obtained for these four angles becomes better at smaller scales, which is consistent with Kraichan's sweeping hypothesis.

The main advantage of the methodology that we present in this work is that it allows one to obtain the energy distribution associated with spatial scales in the plasma frame. The spectral indices determined from power-law fits of the measured frequency spectrum accurately represent the spectral indices associated with the underlying spatial spectrum of turbulent fluctuations in the plasma frame. In spite of a small frequency broadening due to large-scale sweeping, the spatial spectrum can still be recovered to obtain the distribution of fluctuation's energy among scales in the plasma rest frame.

Acknowledgements. J.C.P. was partially supported by NASA grants NNX16AH92G, 80NSSC19K0275 and NSF grant AGS-1752827. SB was supported by NASA grants NNX16AH92G, 80NSSC19K0275 and 80NSSC19K1390. CHKC is supported by STFC Ernest Rutherford Fellowship ST/N003748/2 and STFC Consolidated Grant ST/T00018X/1. Parker Solar Probe was designed, built, and is now operated by the Johns Hopkins Applied

Physics Laboratory as part of NASA's Living with a Star (LWS) program (contract NNN06AA01C). Support from the LWS management and technical team has played a critical role in the success of the Parker Solar Probe mission.

### References

```
Bale, S. D., Goetz, K., Harvey, P. R., et al. 2016, Space Sci. Rev., 204, 49
Bale, S. D., Badman, S. T., Bonnell, J. W., et al. 2019, Nature, 576, 237
Bieber, J. W., Wanner, W., & Matthaeus, W. H. 1996, J. Geophys. Res. Space
   Phys., 101, 2511
Boldyrev, S. 2005, ApJ, 626, L37
Boldyrev, S. 2006, Phys. Rev. Lett., 96, 115002
Bourouaine, S., & Chandran, B. D. G. 2013, ApJ, 774, 96
Bourouaine, S., & Perez, J. C. 2018, ApJ, 858, L20
Bourouaine, S., & Perez, J. C. 2019, ApJ, 879, L16
Bourouaine, S., & Perez, J. C. 2020, ApJ, 893, L32
Bourouaine, S., Alexandrova, O., Marsch, E., & Maksimovic, M. 2012, ApJ, 749,
Bourouaine, S., Perez, J. C., Klein, K. C., et al. 2020, ApJ, 904, L30
Bruno, R., & Carbone, V. 2013, Liv. Rev. Sol. Phys., 10, 2
Chandran, B. D. G. 2008, ApJ, 685, 646
Chen, C. H. K. 2016, J. Plasma Phys., 82, 535820602
Chen, C. H. K., Mallet, A., Yousef, T. A., Schekochihin, A. A., & Horbury, T. S.
   2011, MNRAS, 415, 3219
Chen, C. H. K., Mallet, A., Schekochihin, A. A., et al. 2012, ApJ, 758, 120
Chen, C. H. K., Bale, S. D., Bonnell, J. W., et al. 2020, ApJS, 246, 53
Chen, C. H. K., Chandran, B. D. G., Woodham, L. D., et al. 2021, A&A, 650, L3
   (PSP SI)
Chhiber, R., Usmanov, A. V., Matthaeus, W. H., Parashar, T. N., & Goldstein,
   M. L. 2019, ApJS, 242, 12
Dudok de Wit, T., Krasnoselskikh, V. V., Bale, S. D., et al. 2020, ApJS, 246, 39
Fox, N. J., Velli, M. C., Bale, S. D., et al. 2016, Space Sci. Rev., 204, 7
Goldreich, P., & Sridhar, S. 1995, ApJ, 438, 763
He, G.-W., & Zhang, J.-B. 2006, Phys. Rev. E, 73, 055303
Horbury, T. S., Forman, M., & Oughton, S. 2008, Phys. Rev. Lett., 101, 175005
Howes, G. G., Klein, K. G., & TenBarge, J. M. 2014, ApJ, 789, 106
Huang, S. Y., & Sahraoui, F. 2019, ApJ, 876, 138
Kasper, J. C., Abiad, R., Austin, G., et al. 2016, Space Sci. Rev., 204, 131
Kasper, J. C., Bale, S. D., Belcher, J. W., et al. 2019, Nature, 576, 228
Klein, K. G., Howes, G. G., & TenBarge, J. M. 2014, ApJ, 790, L20
Klein, K. G., Perez, J. C., Verscharen, D., Mallet, A., & Chandran, B. D. G. 2015,
   ApJ, 801, L18
Kraichnan, R. H. 1965, Phys. Fluids, 8, 1385
Lugones, R., Dmitruk, P., Mininni, P. D., Wan, M., & Matthaeus, W. H. 2016,
   Phys. Plasmas, 23, 112304
Martinović, M. M., Klein, K. G., & Bourouaine, S. 2019, ApJ, 879, 43
Mason, J., Cattaneo, F., & Boldyrev, S. 2006, Phys. Rev. Lett., 97, 255002
Matthaeus, W. H., & Goldstein, M. L. 1982, J. Geophys. Res., 87, 6011
Matthaeus, W. H., Dasso, S., Weygand, J. M., Kivelson, M. G., & Osman, K. T.
   2010, ApJ, 721, L10
Matthaeus, W. H., Weygand, J. M., & Dasso, S. 2016, Phys. Rev. Lett., 116,
   245101
Müller, W.-C. & Grappin, R. 2005, Phys. Rev. Lett., 95, 114502
Narita, Y. 2017, Ann. Geophys., 35, 325
Narita, Y., Glassmeier, K.-H., Motschmann, U., & Wilczek, M. 2013, Earth
   Planets Space, 65, e5
Parashar, T. N., Goldstein, M. L., Maruca, B. A., et al. 2020, ApJS, 246, 58 Perez, J. C., & Boldyrev, S. 2009, Phys. Rev. Lett., 102, 025003
Perez, J. C., & Bourouaine, S. 2020, Phys. Rev. Res., 2, 023357
Perez, J. C., Mason, J., Boldyrev, S., & Cattaneo, F. 2012, Phys. Rev. X, 2, 041005
Perez, J. C., Azelis, A. A., & Bourouaine, S. 2020, Phys. Rev. Research, 2, 023189
Perri, S., & Balogh, A. 2010, ApJ, 714, 937
Saur, J., & Bieber, J. 1999, J. Geophys. Res., 104, 9975
Servidio, S., Carbone, V., Dmitruk, P., & Matthaeus, W. H. 2011, Europhys. Lett.,
Taylor, G. I. 1938, Proc. R. Soc. London Ser. A, 164, 476
```

Verma, M. K., Kumar, A., & Gupta, A. 2020, Trans. Indian Natl. Acad. Eng., 5,

Weygand, J. M., Matthaeus, W. H., Kivelson, M. G., & Dasso, S. 2013, J.

Wicks, R. T., Horbury, T. S., Chen, C. H. K., & Schekochihin, A. A. 2010,

Wicks, R. T., Horbury, T. S., Chen, C. H. K., & Schekochihin, A. A. 2011, Phys.

von Papen, M., & Saur, J. 2015, ApJ, 806, 116

Geophys. Res. Space Physi., 118, 3995

Wilczek, M., & Narita, Y. 2012, Phys. Rev. E, 86, 066308

MNRAS, 407, L31

Rev. Lett., 106, 045001

Zhou, Y. 2010, Phys. Rep., 488, 1